

Chemistry A European Journal

 **Chemistry
Europe**
European Chemical
Societies Publishing

Accepted Article

Title: A Small-molecule Diketopyrrolopyrrole-based Dye for in vivo NIR-IIa Fluorescence Bioimaging

Authors: Jianli Hua, Zhicheng Yang, Xiaoxiao Fan, He Li, Xinsheng Li, Sifan Li, Zhiyun Zhang, Hui Lin, and Jun Qian

This manuscript has been accepted after peer review and appears as an Accepted Article online prior to editing, proofing, and formal publication of the final Version of Record (VoR). This work is currently citable by using the Digital Object Identifier (DOI) given below. The VoR will be published online in Early View as soon as possible and may be different to this Accepted Article as a result of editing. Readers should obtain the VoR from the journal website shown below when it is published to ensure accuracy of information. The authors are responsible for the content of this Accepted Article.

To be cited as: *Chem. Eur. J.* 10.1002/chem.202102312

Link to VoR: <https://doi.org/10.1002/chem.202102312>

WILEY-VCH

FULL PAPER

A Small-molecule Diketopyrrolopyrrole-based Dye for *in vivo* NIR-IIa Fluorescence Bioimaging

Zhicheng Yang,^[a] Xiaoxiao Fan,^[b,c] He Li,^[a] Xinsheng Li,^[a] Sifan Li,^[a] Zhiyun Zhang,^[a] Hui Lin,^{*,[b]} Jun Qian,^{*,[b,c]} and Jianli Hua^{*,[a]}

- [a] Dr. Z. Yang, H. Li, X. Li, S. Li, Prof. Z. Zhang, Prof. J. Hua
Key Laboratory for Advanced Materials, Joint International Research Laboratory for Precision Chemistry, School of Chemistry and Molecular Engineering
East China University of Science and Technology
130 Meilong Road, Shanghai 200237, PR China
E-mail: jlhua@ecust.edu.cn
- [b] Dr. X. Fan, Prof. H. Lin, Prof. J. Qian
Department of General Surgery, Sir Run Run Shaw Hospital, School of Medicine
Zhejiang University
866 Yuhangtang Road, Hangzhou 310000, PR China
E-mail: 369369@zju.edu.cn
- [c] Dr. X. Fan, Prof. J. Qian
State Key Laboratory of Modern Optical Instrumentations, Centre for Optical and Electromagnetic Research, College of Optical Science and Engineering,
International Research Center for Advanced Photonics
Zhejiang University
866 Yuhangtang Road, Hangzhou 310058, PR China
E-mail: qianjun@zju.edu.cn
- [†] Z. Y. and X. F. contributed equally.

Supporting information for this article is given via a link at the end of the document.

Abstract: Organic small-molecule fluorophores with near-infrared IIa (NIR-IIa) emission have great potential in pre-clinical detection and inoperative imaging due to the high-spatial resolution and deep penetration. However, developments of the NIR-IIa fluorophores are still facing considerable challenges. In this work, a series of diketopyrrolopyrrole (DPP)-based fluorophores were designed and synthesized. Subsequently, nanomaterial **T25@F127** with significant NIR-IIa emission properties was rationally prepared by encapsulating DPP-based fluorophore **T25**, and was selected for fluorescence angiography and cerebral vascular microscopic imaging with nearly 800 μm penetrating depth and excellent signal-background ratio of 4.07 and 2.26 (at 250 and 400 μm), respectively. Furthermore, the nanomaterial **T25@cRGD** with tumor targeting ability can image tiny metastatic tumor on intestine with a small size of 0.3 mm \times 1.0 mm and high-spatial resolution (SBR = 3.84). This study demonstrates that the nanomaterials which encapsulated **T25** behave as excellent NIR-IIa fluorescence imaging agents and have a great potential for *in vivo* biological application.

Introduction

The fluorescence imaging in near-infrared region (NIR) has emerged as an extremely effective approach for clinical diagnosis and postoperative evaluation.^[1] Comparing with visible and NIR-I biological window, NIR-II (900-1700 nm) fluorescence bioimaging can penetrate deeper tissue with lesser tissue autofluorescence.^[2] The NIR-II window can be further divided into NIR-IIa (1300-1400 nm) and NIR-IIb (1500-1700 nm) sub-regions.^[3] So far, many inorganic and carbon-based materials, including single-walled carbon nanotube (SWNTs), quantum dots and rare-earth nanomaterials, have been developed as NIR-II fluorescent materials.^[4] However, this type of nanomaterials will bring safety issues in terms of immune uptake and biological self-

clearance after *in vivo* imaging, and may also cause potentially long-term toxicity for biological applications. Organic fluorophores possess considerable advantages in terms of biocompatibility and biosafety,^[5] and the fluorescent properties can be adjusted by rational molecular structure designing.^[6] Meanwhile, the development of high-performance NIR-II organic fluorophores are still subject to many restrictions. According to previous reports, many NIR-II fluorophores based on cyanine dyes (such as ICG) exhibit poor photostability and are easily decomposed or isomerized under excitation.^[7] In contrast, compounds that are prone to isomerization may also lead to lower photostability. Thus, fluorophores with rigid conjugated planes should be more stable.^[8] Constructing donor-acceptor-donor (D-A-D) type compounds is another designing strategy for NIR-II fluorophores.^[9] Benzo-bis-thiadiazole (BBTD) is a unique unit with strong electron-withdrawing ability which has been widely used in constructing NIR-II fluorophore as electron-acceptor.^[10] However, irreplaceable electron-acceptor also restricts the variation of D-A-D type NIR-II fluorophore because limited modification can be made. Therefore, researchers have dedicated for designing new types of small organic molecules with NIR-II emission.

Diketopyrrolopyrrole (DPP), as an organic small molecule dye and a planar electron acceptor, is a promising fluorophore for bioimaging with the advantages of good photo- and thermal-stability, high fluorescence quantum yield, wide absorption spectrum, large molar extinction coefficient, strong electron-withdrawing ability, large Stokes shift and easy modification.^[11] Meanwhile, the development of D-A-D type molecule provides a broad platform for DPP-based derivatives. By coupling structural units with different properties (mostly electron donors), a variety of DPP derivatives were synthesized by "building block" manner and widely used for fluorescent sensing,^[12] solar cells,^[13] bioimaging^[14] and other fields.^[15] For example, thiophene substituted DPP derivatives have been considered as strong

FULL PAPER

electron-acceptor and selected for designing organic dyes with long absorption and emission wavelength.^[16] In addition, indeno[1,2-*b*]thiophene with excellent planarity has been regarded as rigid unit to synthesize strong electron donating group and design organic small-molecule dyes by functionalizing 4,4'-dimethoxydiphenylamine,^[17] which can be well used in building dye-sensitized solar cells and NIR fluorophores with broad absorption spectra and excellent photophysical properties.^[18]

Herein, 4,4'-dimethoxydiphenylamine and thiophene-DPP derivatives are combined to construct a D-A-D fluorophore **T14**. In addition, thiophene or indenothiophene is selected as a π bridge which can bond with 4, 4'-dimethoxydiphenylamine to

construct stronger electron-donor. Based on this strategy, fluorophores **T17** and **T25** with longer absorption and emission wavelength are constructed. In order to improve the biocompatibility, the dyes are encapsulated into nanoparticles by Pluronic F127 and used for multiple *in vivo* vascular NIR-IIa bioimaging. Furthermore, nanoparticles **T25@cRGD** with tumor-targeting ability are prepared through encapsulating hydrophobic **T25** by DSPE-PEG₂₀₀₀-cRGD and used for small metastatic tumor NIR-IIa fluorescence imaging. Comparing with previous NIR-II imaging fluorophores, the novel nanomaterial can achieve high-quality NIR-IIa fluorescence imaging with ultra-stability, extraordinary penetrating depth, and high spatial resolution, which shows a great potential in developing *in vivo* bioimaging.

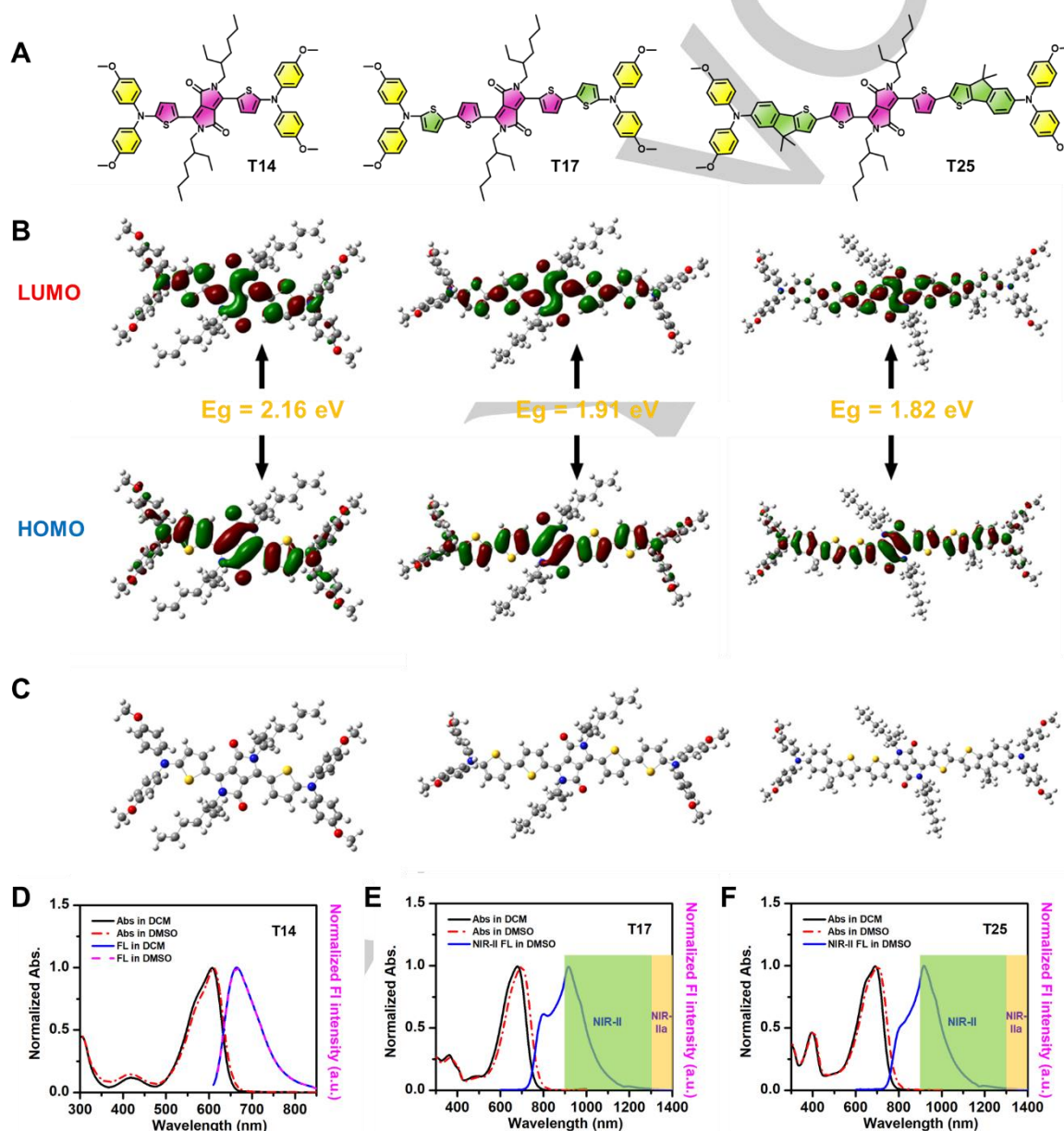


Figure 1. (A) Molecular structures of **T14**, **T17** and **T25**. (B) Energy levels of HOMO and LUMO, energy gaps and electron cloud distributions of **T14**, **T17** and **T25** calculated using the Gaussian 09 program. (C) Optimized ground state (S_0) geometries of the molecules. Normalized UV-vis absorption and fluorescence spectra of compounds. (D) **T14**, (E) **T17** and (F) **T25** in DCM and DMSO solution.

FULL PAPER

Results and Discussion

Design and Synthesis. The **T14** was designed and synthesized by engineering approaches to possess a D-A-D structure, with bis(4-methoxyphenyl)amine as the strong D unit and 2,5-bis(2-ethylhexyl)-3,6-di(thiophen-2-yl)-2,5-dihydropyrrolo[3,4-c]pyrrole-1,4-dione (**SDPP**) as the A unit through Buchwald-Hartwig coupling reaction. In order to broaden the absorption and emission wavelength, stronger electron-donors were designed by combining thiophene or indenothiophene with 4,4'-dimethoxydiphenylamine to construct D-A-D compounds **T17** and **T25**, respectively. The strong electron donors (**3** and **6**) were synthesized by Buchwald-Hartwig coupling reaction between bis(4-methoxyphenyl)amine and 2-bromothiophene or 6-chloro-4,4-dimethyl-4*H*-indeno[1,2-*b*]thiophene, respectively. Then, the intermediates **3** or **6** were further used to synthesize organotin compounds and the finally combined with **SDPP** by Stille coupling reaction. All new compounds were well-confirmed by ¹H nuclear magnetic resonance (NMR), ¹³C NMR spectroscopies and high-resolution mass spectrometry (HRMS).

Photophysical Properties. Primarily, the molecular structures of fluorophores were shown **Figure 1A**. **T14** exhibits a maximum absorption and emission wavelength at 610 nm and 665 nm, respectively, with violet color and red fluorescence and molar extinction coefficient of $2.30 \times 10^4 \text{ M}^{-1} \text{ cm}^{-1}$ (**Figure 1D and S10**). As a typical D-A-D compound, **T14** presents long-wavelength absorption and NIR-I region (650-900 nm) fluorescence emission with strong emission intensity. However, the emission wavelength of **T14** cannot extend to the NIR-II region. Therefore, thiophene or indenothiophene coupling with 4,4'-dimethoxydiphenylamine is selected for molecular design as stronger electron donor to synthesize **T17** and **T25**, respectively. As we expected, the maximum absorption peak of **T17** and **T25** locate at 700 nm with high molar extinction coefficient of 5.37×10^4 and $7.15 \times 10^4 \text{ M}^{-1} \text{ cm}^{-1}$, respectively (**Figure 1E-F, S10**), which red shifted ~100 nm comparing with **T14**. Meanwhile, **T17** and **T25** exhibit strong NIR-II emission with the maximum emission peak at 900 nm, and the cut-off emission wavelength exceeding over 1300 nm. And the fluorescence quantum yield (QY) of **T25** in DMSO was 14.10% (range of 800-1300 nm). Comparing with **T14**, the maximum emission peaks of **T17** and **T25** red shifted ~250 nm, which highlights the importance of the stronger electron-donor in the molecular design (**Figure 1D-F**). In addition, after continuously irradiation for 20 min (Laser 690 nm, 400 mW/cm²), barely changes can be observed in the UV absorption spectrum of **T25**, indicating the excellent photostability of **T25** comparing with **T17** (**Figure S11-12**).

In order to clarify the relationship between the molecular structure and photophysical properties of **T14**, **T17** and **T25**, density functional theory (DFT) calculation was carried out by Gaussian 09 program to obtain the energy levels and spatial configurations of molecular orbitals. The highest occupied molecular orbitals (HOMOs), lowest unoccupied molecular orbitals (LUMOs), energy levels and ground state spatial configurations of the three compounds are shown in **Figure 1B-C**. The HOMO-LUMO energy level difference (*E_g*) of compounds **T14**, **T17** and **T25** are 2.16 eV, 1.91 eV and 1.82 eV, respectively, which can correspond to the absorption spectrum and the electron-donating ability of different electron donor. Obviously, LUMOs of **T14**, **T17**, and **T25**

are mainly distributed on the electron acceptor **SDPP**, while HOMOs are almost delocalized along the whole backbone, indicating the intramolecular charge transfer (ICT) of the fluorophores. Comparing with **T14**, the decreasing energy gaps (*E_g*) between HOMO and LUMO of **T17** and **T25** are due to the increasing electron donating ability of donor and strengthening ICT effects, which can be clearly observed in HOMO diagrams.

Characterization and *In vitro* Imaging of Nanoparticles. In order to improve the biocompatibility, **T14**, **T17** and **T25** were encapsulated into nanoparticles by Pluronic F127 through nanoprecipitation (**Figure 2A**). The morphologies of **T14@F127**, **T17@F127** and **T25@F127** were revealed by transmission electron microscopy (TEM) as a spherical shape. The sizes of the nanoparticles were obtained by Malvern dynamic light scattering (DLS) with diameters of ~30 nm (**Figure 2B-D**). During storage at 4 °C for 20 days, no obvious variations of the Z-Average and polymer dispersity index (PDI) were observed (**Figure S14**), indicating excellent stability of these nanoparticles.

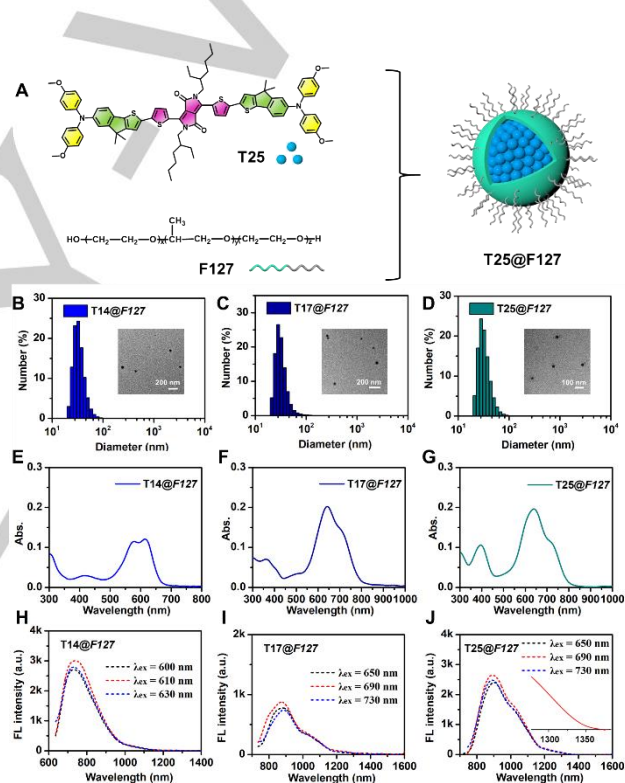


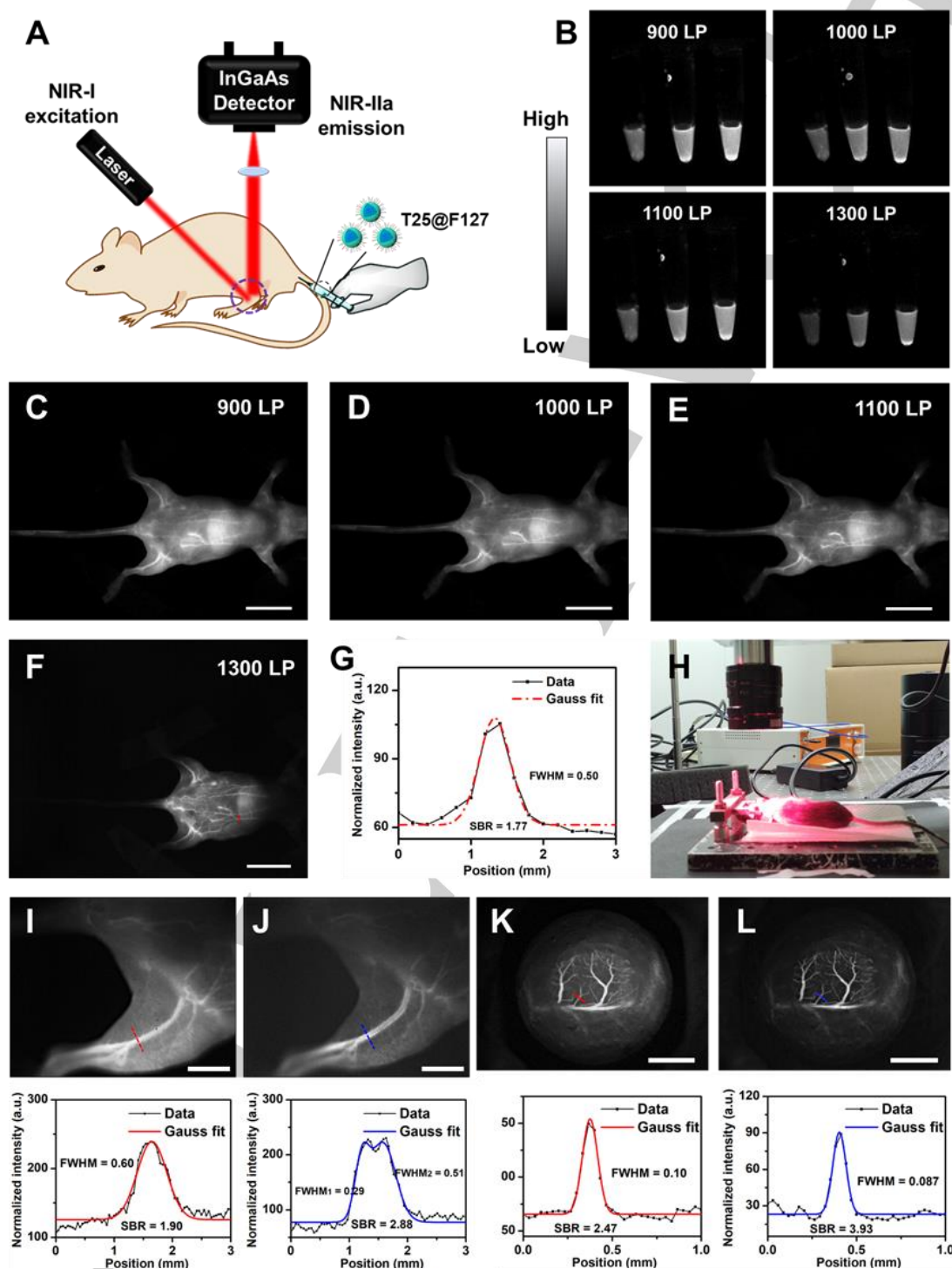
Figure 2. (A) Schematic illustration of **T25** encapsulating to nanoparticles by Pluronic F127. The DLS spectrum of (B) **T14@F127**, (C) **T17@F127** and (D) **T25@F127** (inset picture: TEM image of nanoparticles). UV-vis absorption spectra of (E) **T14@F127**, (F) **T17@F127** and (G) **T25@F127**. Fluorescence emission spectra of (H) **T14@F127**, (I) **T17@F127** and (J) **T25@F127**.

After encapsulated into nanoparticles, the color and absorption spectra of solution presented negligible variation. As shown in **Figure 2E-G**, the maximum emission peaks of **T17@F127** and **T25@F127** are located at ~880 nm and ~900 nm, respectively. The fluorescence intensity of **T17@F127** or **T25@F127** excited at 690 nm is slightly higher than the other two wavelengths with the Stokes shift of ~200 nm (**Figure 2H-J**). The NIR-II fluorescence emission intensity of **T25@F127** is significantly stronger than that of **T17@F127**, and the fluorescence emission can exceed 1300

FULL PAPER

nm to reach the NIR-IIa imaging region with the QY of 1.84% (range of 800-1400 nm) which made **T25@F127** more advantageous for biological imaging. In addition, the chemical stability of **T25@F127** has been assessed in the presence of different inorganic salts (NaCl, KNO₃, MgSO₄, NaNO₂), reactive

oxygen (H₂O₂, ClO⁻) and sulfur species (cysteine, homocysteine and glutathione), and negligible alteration of NIR-II emission has been observed indicating good chemical stability of **T25@F127** (Figure S13). Thus, **T25@F127** with excellent properties was selected for further *in vivo* biological application.



FULL PAPER

Before the further application in bioimaging, the *in vitro* imaging of **T25@F127** was captured by an InGaAs detector. As shown in **Figure 3B**, under the excitation of a 690 nm laser (50 mW/cm²), **T25@F127** with different concentrations (0.1, 0.25, 0.5 mg/mL) emit strong NIR-II emission signal through 900 nm (25 ms), 1000 nm (25 ms) and 1100 nm (39 ms) long-pass (LP) filter. Interestingly, distinctive emission signals can be observed through 1300 nm (75 ms) and 1500 nm (150 ms) LP filter (**Figure 3B, S16**), which implied its potential for NIR-IIa fluorescence bioimaging.

Blood Vessel Imaging. Primarily, the biocompatibility and cytotoxicity of **T25@F127** was evaluated by MTT assay before the *in vivo* imaging. L02 cell line (normal liver cells) and CT26 cell line (mice colon cancer cells) were selected for the MTT assay. As shown in **Figure S15**, L02 and CT26 cells exhibited high viability of 90% after incubating **T25@F127** with a concentration of 100 µg/mL, which indicated the excellent biocompatibility and potential for biological applications.

By intravenously injecting **T25@F127**, fluorescence angiography can be realized as a non-radioactive imaging strategy. Thus, NIR-II and NIR-IIa fluorescence images of whole-body blood vessels in nude mice were acquired through different filters (900-1300 nm) after intravenously injection of **T25@F127** (200 µL, 0.5 mg/mL). As shown in **Figure 3D-G**, with the wavelength of the LP filter increases, the spatial resolution of images was significantly improved. In the fluorescence images captured in NIR-IIa biological window, higher resolution angiography images of mouse can be clearly distinguished with a Gaussian-fitted full width at half maximum (FWHM) of 0.50 mm and signal to background ratio (SBR) of 1.77.

To observe the details of blood vessels, we increased the distance between camera and camera lens, and enlarged images could be acquired (**Figure 3H**). In order to further verify the advantages of NIR-IIa fluorescence imaging, the hind-limb blood vessels of nude mice were selected for analysis. As shown in **Figure 3I**, the NIR-II fluorescent image (1100 nm LP filter) performed clear morphology of blood vessels. To assess the quality of NIR-II fluorescence imaging, a line was drawn across the femoral vessels and Gauss-fitted analysis was performed. The FWHM of femoral vessel was 0.60 mm, and the SBR of femoral vessel was 1.90. Unexpectedly, the femoral artery and femoral vein, which are very close and difficult to distinguish from each other by the 1100 nm LP filter, can be clearly observed in the NIR-IIa biological window (1300 nm LP filter) with higher resolution (Femoral artery, FWHM₁ = 0.29 mm, Femoral vein, FWHM₂ = 0.51 mm, SBR = 2.88).

Furthermore, the craniotomy mice were used for cerebral blood vessels NIR-II and NIR-IIa fluorescence imaging. As shown in **Figure 3K**, due to the high SBR of bioimaging in NIR-II biological window (1100 nm LP), the cerebral blood vessels can be imaged clearly by InGaAs detector (FWHM = 100 µm, SBR = 2.47) after intravenously injection of **T25@F127** (200 µL, 500 µg/mL). In the NIR-IIa fluorescence imaging (1300 nm LP) of cerebral blood vessels (**Figure 3L**), the same cerebrovascular performed higher spatial resolution (FWHM = 87 µm, SBR = 3.93), which also proves that the imaging in NIR-IIa region can exhibit better clarity and resolution compared to that in traditional NIR-II region.

High-Spatial-Resolution Cerebral Vascular Microscopic NIR-IIa Fluorescence Imaging. The scientific researches of cerebrovascular are inextricably related to neuroinformatics and diagnosis of neurological disorders, including Alzheimer's disease and dysfunction of cerebrovascular. Angiography in NIR-IIa biological window provides us a powerful tool to observe the brain blood vessels clearly through the thick tissue. After intravenously injecting **T25@F127** (200 µL, 0.5 mg mL⁻¹), the imaging of cerebrovascular network in mouse with a cranial window can be clearly acquired. The NIR-IIa fluorescence signals of cerebral vessels at various vertical depths can be recorded ranging from 0 µm to nearly 800 µm by regulating the relative position between the sample stage and objective lens.

The system of NIR-II fluorescence microscopic imaging was presented in **Figure 4A** and reported in our previous study.^[19] As shown in **Figure 4**, by 1300 nm LP filter, NIR-IIa images of cerebral vessels are easily captured. In the NIR-IIa images at depth of 250 µm, the cerebrovascular can be imaged clearly with excellent FWHM and SBR of 3.96 µm and 4.07, respectively. Even penetrating a deeper depth of 400 µm, the cerebrovascular structure was rich and could be discriminated easily with high spatial resolution (FWHM = 3.90 µm, SBR = 2.26). Taking the advantages of bioimaging in NIR-IIa region, **T25@F127** exhibits extraordinary performance in cerebrovascular microscopic imaging.

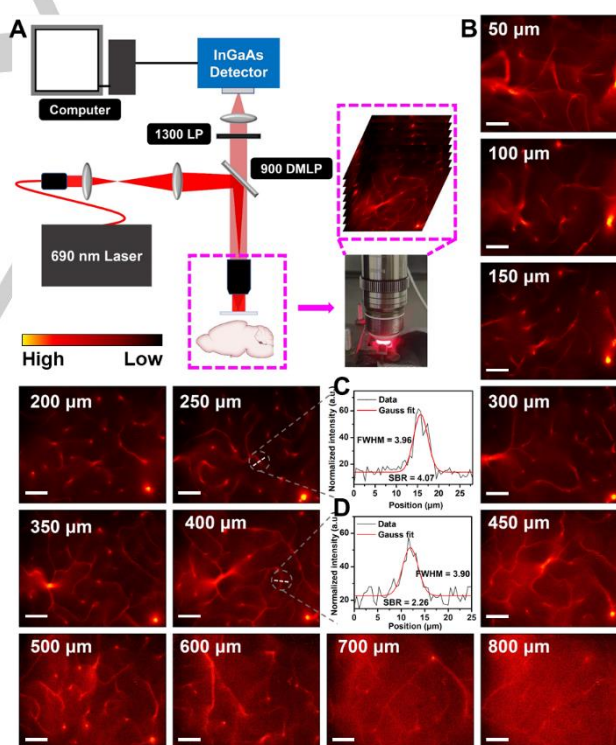


Figure 4. (A) Schematic illustration of NIR-IIa fluorescence imaging of the cerebral vascular in the C57BL/6 mice by microscopic imaging system. (B) The NIR-IIa images (50-800 µm) of the cerebral vessels at various depths in the C57BL/6 mouse by microscopic imaging system. Scale bar = 50 µm. The Gaussian fitting to the profile of white line at (C) 250 µm and (D) 400 µm, which showed high spatial resolutions.

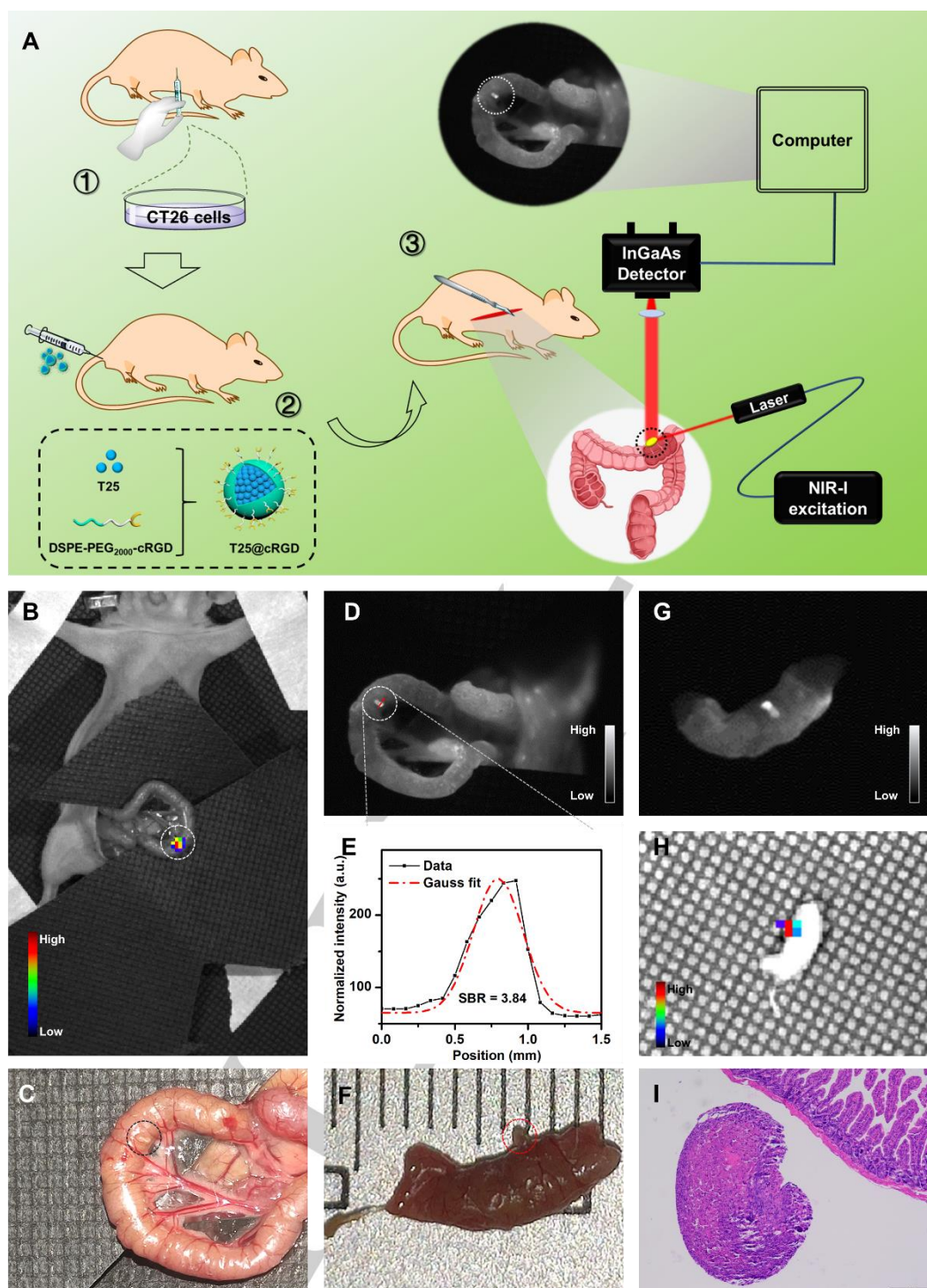


Figure 5. (A) Schematic illustration of NIR-IIa fluorescence image of the small metastatic tumor on intestine. (B) The luciferase imaging of the tumor. (C) The picture of the small metastatic tumor (black circle). (D) The NIR-IIa fluorescence imaging of the tumor on intestine wall (white circle). (E) The fluorescence intensity profiles (black line) and Gaussian fit (red dashed line) along the red line in in Fig. 5D (white circle). (F) The picture of the tumor on the resected intestine (red circle). (G) The NIR-IIa fluorescence imaging of tumor on the resected intestine. (H) The luciferase imaging of the tumor on the resected intestine. (I) The H&E staining.

NIR-IIa Fluorescence Imaging of Small Metastatic Tumor in Abdominal Cavity. During the process of clinical tumor resection, the precise differentiation and complete removal of tumor nodules plays a very important role in improving the quality of surgery. Traditionally, the quality of surgery is determined mainly by the

experience of the surgeons. The emergence of fluorescence imaging-guided surgery, especially imaging in NIR region, bring the surgical field into a new era.^[20] Compared to fluorescence imaging in NIR-I region, fluorescence imaging in NIR-II region offers higher spatial resolution and is a better option for surgical

FULL PAPER

navigation. Therefore, NIR-IIa imaging with even higher SBR provides us an appropriate approach for clinical imaging-guided surgery. The nude mice were pre-treated with the suspension of luciferase-transfected CT26 cells (mice colon cancer cells) by intraperitoneal injection to establish peritoneal metastasis tumor mouse models. At the day 4, obvious luciferase signals could be detected *in vivo* which indicated the formation of tumor. According to previous report, targeting tumors via cRGD conjugated nanocarriers have emerged as a promising technique for delivering nanoparticles for cancer theranostics.^[21] **T25** is further encapsulated by DSPE-PEG₂₀₀₀-cRGD to form **T25@cRGD** nanoparticles with actively targeted ability to tumor. **T25@cRGD** exhibits NIR-IIa emission with homogeneous nanoparticle diameter (**Figure S17**).

After intravenous injection of **T25@cRGD** (200 μ L, 0.5 mg/mL) for 24 h, the nanoparticles could enrich in small tumor on the small intestine of the mouse by synthetic effect of positive-targeting ability and EPR effect. The mouse was then anesthetized and underwent laparotomy. As shown in **Figure 5D-E**, the small tumor nodule at the surface of small intestine has been clearly captured by NIR-IIa fluorescence imaging system with the SBR of 3.84. The intestinal segment with a small tumor was then resected and further verified the NIR-IIa fluorescence and luciferase signals *in vitro* (**Figure 5G-H**).

In the NIR-IIa image of tumor tissue, a tiny nodule with size of 0.3 mm \times 1.0 mm was incredibly distinguished which was hard to identify by naked eyes (**Figure 5C and 5F**). To further confirm the tumor in pathological level, the small nodule was harvested and sectioned into slices. Hematoxylin and eosin (H&E) staining was then performed and verified that the small nodule was malignant (**Figure 5I**).

Conclusion

In summary, a novel small-molecule DPP-based fluorophore **T25** with NIR-I absorption and NIR-II emission was rationally designed and synthesized. Based on the promising properties of **T25**, nanoparticles **T25@F127** with NIR-IIa emission were effectively constructed by encapsulating fluorophore **T25** using Pluronic F127, which exhibited excellent biocompatibility, good chemical stability, and extraordinary fluorescence property. Under a 690 nm laser excitation, **T25@F127** emitted strong fluorescent in NIR-II and NIR-IIa window through 900 and 1300 nm LP filter, respectively. By intravenous injection of **T25@F127** into mice, the systemic, the femoral and cerebral vessels were clearly captured with high resolution in NIR-IIa imaging window. In addition, taking the extraordinary performance of NIR-IIa imaging by **T25@F127**, the cerebrovascular network of mouse was recorded within nearly 800 μ m depth by high-spatial-resolution NIR-IIa fluorescence microscopic imaging and captured excellent SBR of 4.07 and 2.26 at 250 μ m and 400 μ m depth, respectively. By intravenous injection of **T25@cRGD**, the size and location of small metastatic tumor (0.3 mm \times 1.0 mm) could be accurately observed via NIR-IIa fluorescence imaging with high spatial resolution. Thanks to the outstanding NIR-IIa fluorescence performance of **T25** nanoparticles, *in vivo* imaging studies is likely to lead further clinical biological applications, including cerebrovascular health assessment and imaging-guided surgery. More importantly, this

work provides us a new strategy for the design and synthesis of small-molecule dyes for NIR-II fluorescence imaging.

Experimental Section

Materials. All reagents were bought from commercial sources (Energy Chemical, Sigma-Aldrich, TCI) and used without further processing. DSPE-PEG₂₀₀₀-cRGD was purchased from biological technology company (Xi'an ruixi, China). All solvents were purified and dried before using by standard methods. The solvents used in spectrum analysis were of HPLC grade. The solutions for analytical studies were pre-prepared with deionized water treated using a Milli-Q System (Billerica, MA, USA).

Instruments. ¹H NMR and ¹³C NMR spectra were recorded on a Bruker AM-400 MHz NMR spectrometer. Chemical shifts were expressed in ppm (in chloroform-*d* (CDCl₃) and DMSO-*d*₆; TMS as an internal standard) and coupling constants (*J*) in Hz. Electrospray ionization and time-of-flight analyzer (ESI-TOF) mass spectra were determined using a Waters Micromass LCT mass spectrometer. Absorption spectra were recorded on a P Varian Cary 500 UV-vis spectrophotometer. The NIR-II fluorescence and absolute fluorescence quantum yield were recorded by Edinburgh Instruments Fluorescence Spectrometer FLS1000 with integrating sphere measurement. NIR-II imaging of living mouse was collected using an InGaAs camera (TEKWIN SYSTEM, China, 900–1700 nm sensitive) with a 690 nm laser as an excitation.

Density Functional Theory Calculation Methodology. Geometry optimizations were carried out on the molecules in the gas phase, using the Gaussian view to enter the starting geometry. The molecules were distorted to form a variety of conformers which were then allowed to optimize, in order to find the global minimum on the potential energy surface. Frequency calculations were performed on all the optimized geometries to distinguish whether they were minima or transition states on the potential energy surfaces. Where transition state geometries were found, the bond lengths and angles were distorted in the direction of the vibration and the structure was reoptimized until only positive frequencies were obtained. All calculations were carried out using the Gaussian 09 program^[22] with the B3LYP functional and the standard 6-31G(d, p) basis set.

Preparation of Nanoparticles. The synthetic processes of **T14**, **T17** and **T25** are exhibited in **Scheme S1**, Supporting Information. **T14** (1.0 mg) and Pluronic F127 (10 mg) was dissolved in THF (1.5 mL). And the mixture was dropwise added into stirring deionized water (5 mL) and kept stirring for 3 h to evaporated THF. Water-dispersed **T14@F127** was obtained afterwards. **T17@F127**, **T25@F127** and **T25@cRGD** were obtained by similar approaches.

Cell Lines and Cell Culture. Mouse colon cancer cell line (CT26) was purchased from the Type Culture Collection of the Chinese Academy of Sciences (Shanghai, China). L02 normal liver cell line was kindly provided by Cang Yong's lab, Zhejiang University. CT26 cell line and L02 were cultured in RPMI-1640 (Gibco, Cat. No. C11975500BT) supplemented with 10% FBS (Cellmax, Cat. No. SA102.02) and maintained at 37 °C with 5% CO₂.

Establishment of a Luciferase-Transfected CT26 Cell Line. The lentivirus (pHBLV-Luc-Puro, lot number: 45070327) was purchased from Hanbio. CT26 cells were precultured at a density of 1 \times 10⁵ cells in six-well plate. pHBLV-Luc-Puro virus was added at a multiplicity of infection (MOI) of 20. CT26 cancer cells were then cultured for 24 h and further selected with 2 μ g mL⁻¹ puromycin for 3 d.

In Vitro Cytotoxicity. To evaluate the biocompatibility and security of **T25@F127**, the cytotoxicity to CT26 and L02 cells was evaluated by MTT assays. CT26 and L02 cells were cultured on 96-well plates at 37 °C for

FULL PAPER

12 h. Then, **T25@F127** with various concentrations (2, 5, 10, 25, 50, and 100 $\mu\text{g/mL}$) were added and incubated for 24 h. After replacing the culture medium, MTT (20 μL , 5 mg/mL in PBS) was added to each cell and incubated for 3 hours. The absorbance was determined using a multifunctional microplate reader (Synergy H1, BioTek Instruments, America) at 470 nm. The relative cell survival rate (%) was calculated by the following formula: cell survival rate = $(\text{OD}_{\text{treated}}/\text{OD}_{\text{control}}) \times 100\%$.

Animal Models. The female nude mice (6 weeks old) and C57BL/6 mice used in this study were obtained from the Laboratory Animal Center of Zhejiang University, and all *in vivo* experiments were carried out in compliance with the Zhejiang University Animal Study Committee's requirements for the care and use of laboratory animals in research.

NIR-II Fluorescence Whole-Body Imaging. Nude mice (18–22 g, $n = 3$ for each group) were chosen for NIR-II fluorescence whole-body imaging. After the intravenous injection of **T25@F127** (250 μL , 0.5 mg/mL), the mice were anesthetized with pentobarbital at various time points post-injection and imaged with the NIR-II fluorescence whole-body imaging system. The images were obtained upon excitation at 690 nm and signal collection using a 900, 1000, 1100 or 1300 nm LP filter, respectively.

NIR-II fluorescence microscopic imaging. As shown in **Figure 5A**, a 690 nm laser beam utilized as the excitation source. After passing through a 900 nm long-pass dichroic mirror and an air objective lens (LSM03, WD = 25.1 mm, Thorlabs), an infrared transmission water-immersed object (XLPLN25XWMP2, 25 \times , NA = 1.05, Olympus), the 690 nm laser illuminated on the samples. NIR-II fluorescence signals were collected by the same objective, and recorded with the InGaAs camera.

Acknowledgements

For financial support of this research, we thank the project supported by the National Natural Science Foundation of China (21788102, 21772040, 21971064 and 91859205), Shanghai Municipal Science and Technology Major Project (Grant No.2018SHZDZX03), the Fundamental Research Funds for the Central Universities (222201717003 and 50321101918001) and the Programme of Introducing Talents of Discipline to Universities (B16017). The authors thank Research Center of Analysis and Test of East China University of Science and Technology for the help on the characterization.

Keywords: NIR-IIa imaging • small-molecule • diketopyrrolopyrrole • fluorescence angiography • metastatic tumor diagnosis

- [1] a) F. Ding, Y. Zhan, X. Lu, Y. Sun, *Chem. Sci.* **2018**, *9*, 4370–4380; b) S. Zhu, R. Tian, A. L. Antaris, X. Chen, H. Dai, *Adv. Mater.* **2019**, *31*, 1900321; c) Y. Yang, Y. Yu, H. Chen, X. Meng, W. Ma, M. Yu, Z. Li, C. Li, H. Liu, X. Zhang, H. Xiao, Z. Yu, *ACS Nano* **2020**, *14*, 13536–13547.
- [2] a) G. Xu, Q. Yan, X. Lv, Y. Zhu, K. Xin, B. Shi, R. Wang, J. Chen, W. Gao, P. Shi, C. Fan, C. Zhao, H. Tian, *Angew. Chem. Int. Ed.* **2018**, *57*, 3626–3630; b) Z. Hu, C. Fang, B. Li, Z. Zhang, C. Cao, M. Cai, S. Su, X. Sun, X. Shi, C. Li, T. Zhou, Y. Zhang, C. Chi, P. He, X. Xia, Y. Chen, S. S. Gambhir, Z. Cheng, J. Tian, *Nat. Biomed. Eng.* **2020**, *4*, 259–271; c) Y. Suo, F. Wu, P. Xu, H. Shi, T. Wang, H. Liu, Z. Cheng, *Adv. Healthc. Mater.* **2019**, *8*, 1900974; d) Z. Deng, S. Bi, M. Jiang, S. Zeng, *ACS Nano* **2021**, *15*, 3201–3211.
- [3] a) Y. Li, Z. Cai, S. Liu, H. Zhang, S. T. H. Wong, J. W. Y. Lam, R. T. K. Kwok, J. Qian, B. Z. Tang, *Nat. Commun.* **2020**, *11*, 1255; b) W. Wu, Y. Yang, Y. Yang, Y. Yang, K. Zhang, L. Guo, H. Ge, X. Chen, J. Liu, H. Feng, *Small* **2019**, *15*, 1805549.
- [4] a) X. Zhang, L. An, Q. Tian, J. Lin, S. Yang, *J. Mater. Chem. B* **2020**, *8*, 4738–4747; b) Y. Cai, Z. Wei, C. Song, C. Tang, W. Han, X. Dong, *Chem. Soc. Rev.* **2019**, *48*, 22–37; c) L. Li, Z. Zeng, Z. Chen, R. Gao, L. Pan, J. Deng, X. Ye, J. Zhang, S. Zhang, C. Mei, J. Yu, Y. Feng, Q. Wang, A. Y. Yu, M. Yang, J. Huang, *ACS Nano* **2020**, *14*, 15403–15416.
- [5] a) Z. Sheng, Y. Li, D. Hu, T. Min, D. Gao, J. S. Ni, P. Zhang, Y. Wang, X. Liu, K. Li, H. Zheng, B. Z. Tang, *Research (Wash D C)* **2020**, *2020*, 4074593; b) D. Li, C. Qu, Q. Liu, Y. Wu, X. Hu, K. Qian, B. Chang, S. He, Y. Yuan, Y. Li, T. Ko, A. Yu, Z. Cheng, *Adv. Funct. Mater.* **2019**, *30*, 1906343; c) Q. Liu, J. Tian, Y. Tian, Q. Sun, D. Sun, F. Wang, H. Xu, G. Ying, J. Wang, A. K. Yetisen, N. Jiang, *ACS Nano* **2021**, *15*, 515–525.
- [6] a) Y. Su, B. Yu, S. Wang, H. Cong, Y. Shen, *Biomaterials* **2021**, *271*, 120717; b) Z. Sheng, B. Guo, D. Hu, S. Xu, W. Wu, W. H. Liew, K. Yao, J. Jiang, C. Liu, H. Zheng, B. Liu, *Adv. Mater.* **2018**, 1800766; c) J. Ouyang, L. Sun, Z. Zeng, C. Zeng, F. Zeng, S. Wu, *Angew. Chem. Int. Ed.* **2019**, *59*, 10111–10121; d) W. Xu, D. Wang, B. Z. Tang, *Angew. Chem. Int. Ed.* **2021**, *60*, 7476–7487; e) Z. Lei, F. Zhang, *Angew. Chem. Int. Ed.* **2021**, *60*, 16294–16308.
- [7] E. D. Cosco, J. R. Caram, O. T. Bruns, D. Franke, R. A. Day, E. P. Farr, M. G. Bawendi, E. M. Sletten, *Angew. Chem. Int. Ed.* **2017**, *56*, 13126–13129.
- [8] a) Z. Lei, C. Sun, P. Pei, S. Wang, D. Li, X. Zhang, F. Zhang, *Angew. Chem. Int. Ed.* **2019**, *58*, 8166–8171; b) B. Li, L. Lu, M. Zhao, Z. Lei, F. Zhang, *Angew. Chem. Int. Ed.* **2018**, *57*, 7483–7487.
- [9] a) R. Tian, H. Ma, S. Zhu, J. Lau, R. Ma, Y. Liu, L. Lin, S. Chandra, S. Wang, X. Zhu, H. Deng, G. Niu, M. Zhang, A. L. Antaris, K. S. Hettie, B. Yang, Y. Liang, X. Chen, *Adv. Mater.* **2020**, *32*, 1907365; b) H. Ma, C. Liu, Z. Hu, P. Yu, X. Zhu, R. Ma, Z. Sun, C.-H. Zhang, H. Sun, S. Zhu, Y. Liang, *Chem. Mater.* **2020**, *32*, 2061–2069; c) S. Liu, C. Chen, Y. Li, H. Zhang, J. Liu, R. Wang, S. T. H. Wong, J. W. Y. Lam, D. Ding, B. Z. Tang, *Adv. Funct. Mater.* **2019**, *30*, 1908125; d) S. Li, H. Chen, H. Liu, L. Liu, Y. Yuan, C. Mao, W. Zhang, X. Zhang, W. Guo, C. S. Lee, X. J. Liang, *ACS Nano* **2020**, *14*, 13681–13690.
- [10] a) A. L. Antaris, H. Chen, K. Cheng, Y. Sun, G. Hong, C. Qu, S. Diao, Z. Deng, X. Hu, B. Zhang, X. Zhang, O. K. Yaghi, Z. R. Alamparambil, X. Hong, Z. Cheng, H. Dai, *Nat. Mater.* **2016**, *15*, 235–242; b) C. Qu, Y. Xiao, H. Zhou, B. Ding, A. Li, J. Lin, X. Zeng, H. Chen, K. Qian, X. Zhang, W. Fang, J. Wu, Z. Deng, Z. Cheng, X. Hong, *Adv. Opt. Mater.* **2019**, *7*, 1900229. c) A. L. Antaris, H. Chen, S. Diao, Z. Ma, Z. Zhang, S. Zhu, J. Wang, A. X. Lozano, Q. Fan, L. Chew, M. Zhu, K. Cheng, X. Hong, H. Dai, Z. Cheng, *Nat. Commun.* **2017**, *8*, 15269.
- [11] a) T. He, Y. Gao, S. Sreejith, X. Tian, L. Liu, Y. Wang, H. Joshi, S. Z. F. Phua, S. Yao, X. Lin, Y. Zhao, A. C. Grimsdale, H. Sun, *Adv. Opt. Mater.* **2016**, *4*, 746–755; b) Y. Liu, Z. Qu, H. Cao, H. Sun, Y. Gao, X. Jiang, *ACS Nano* **2017**, *11*, 12446–12452.
- [12] a) F. Wu, L. Wang, H. Tang, D. Cao, *Anal. Chem.* **2019**, *91*, 5261–5269; b) Y. Hang, J. Wang, T. Jiang, N. Lu, J. Hua, *Anal. Chem.* **2016**, *88*, 1696–1703.
- [13] a) A. Tang, C. Zhan, J. Yao, E. Zhou, *Adv. Mater.* **2017**, *29*, 1600013. b) X. Song, N. Gasparini, M. M. Nahid, S. H. K. Paleti, C. Li, W. Li, H. Ade, D. Baran, *Adv. Funct. Mater.* **2019**, *29*, 1902441.
- [14] a) K. Shou, Y. Tang, H. Chen, S. Chen, L. Zhang, A. Zhang, Q. Fan, A. Yu, Z. Cheng, *Chem Sci* **2018**, *9*, 3105–3110; b) Q. Wang, Y. Dai, J. Xu, J. Cai, X. Niu, L. Zhang, R. Chen, Q. Shen, W. Huang, Q. Fan, *Adv. Funct. Mater.* **2019**, *29*, 1901480; c) Y. Gao, G. Feng, T. Jiang, C. Goh, L. Ng, B. Liu, B. Li, L. Yang, J. Hua, H. Tian, *Adv. Funct. Mater.* **2015**, *25*, 2857–2866.
- [15] a) Y. Cai, P. Liang, Q. Tang, X. Yang, W. Si, W. Huang, Q. Zhang, X. Dong, *ACS Nano* **2017**, *11*, 1054–1063; b) J. Zou, J. Zhu, Z. Yang, L. Li, W. Fan, L. He, W. Tang, L. Deng, J. Mu, Y. Ma, Y. Cheng, W. Huang, X. Dong, X. Chen, *Angew. Chem. Int. Ed.* **2020**, *59*, 8833–8838; c) K. Narayanaswamy, B. Yadagiri, A. Bagui, V. Gupta, S. P. Singh, *Eur. J. Org. Chem.* **2017**, *2017*, 4896–4904.
- [16] a) Q.-R. Yin, J.-S. Miao, Z. Wu, Z.-F. Chang, J.-L. Wang, H.-B. Wu, Y. Cao, *J. Mater. Chem. A* **2015**, *3*, 11575–11586; b) Y. Lyu, J. Zeng, Y. Jiang, X. Zhen, T. Wang, S. Qiu, X. Lou, M. Gao, K. Pu, *ACS Nano* **2018**, *12*, 1801–1810.
- [17] H. Ding, Y. Chu, M. Xu, S. Zhang, H. Ye, Y. Hu, J. Hua, *J. Mater. Chem. C* **2020**, *8*, 14864–14872.

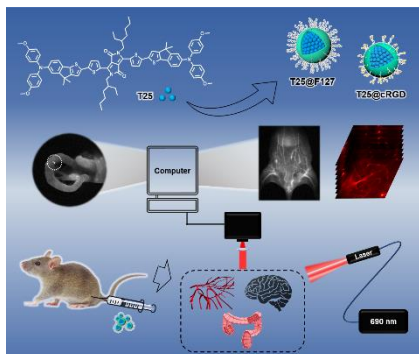
FULL PAPER

- [18] Z. Shen, B. Xu, P. Liu, Y. Hu, Y. Yu, H. Ding, L. Kloo, J. Hua, L. Sun, H. Tian, *J. Mater. Chem. A* **2017**, *5*, 1242–1247.
- [19] Z. Feng, X. Yu, M. Jiang, L. Zhu, Y. Zhang, W. Yang, W. Xi, G. Li, J. Qian, *Theranostics* **2019**, *9*, 5706–5719.
- [20] X. Fan, Y. Li, Z. Feng, G. Chen, J. Zhou, M. He, L. Wu, S. Li, J. Qian, H. Lin, *Adv. Sci.* **2021**, *8*, 2003972.
- [21] a) J. Choi, J. Yang, J. Park, E. Kim, J. S. Suh, Y. M. Huh, S. Haam, *Adv. Funct. Mater.* **2011**, *21*, 1082–1088; b) C. Wang, Y. Chen, Z. Xu, B. Chen, Y. Zhang, X. Yi, J. Li, *Sen. Actuators B Chem.* **2020**, *309*, 127732; c) X. Hu, X. Guan, J. Li, Q. Pei, M. Liu, Z. Xie, X. Jing, *Chem. Commun.* **2014**, *50*, 9188–9191.
- [22] Revision A.02 ed. (Ed.: G. W. T. M. J. Frisch, H. B. Schlegel, G. E. Scuseria, M. A. Robb, J. R. Cheeseman, G. Scalmani, V. Barone, G. A. Petersson, H. Nakatsuji, X. Li, M. Caricato, A. Marenich, J. Bloino, B. G. Janesko, R. Gomperts, B. Mennucci, H. P. Hratchian, J. V. Ortiz, A. F. Izmaylov, J. L. Sonnenberg, D. Williams-Young, F. Ding, F. Lipparini, F. Egidi, J. Goings, B. Peng, A. Petrone, T. Henderson, D. Ranasinghe, V. G. Zakrzewski, J. Gao, N. Rega, G. Zheng, W. Liang, M. Hada, M. Ehara, K. Toyota, R. Fukuda, J. Hasegawa, M. Ishida, T. Nakajima, Y. Honda, O. Kitao, H. Nakai, T. Vreven, K. Throssell, J. A. Montgomery, Jr., J. E. Peralta, F. Ogliaro, M. Bearpark, J. J. Heyd, E. Brothers, K. N. Kudin, V. N. Staroverov, T. Keith, R. Kobayashi, J. Normand, K. Raghavachari, A. Rendell, J. C. Burant, S. S. Iyengar, J. Tomasi, M. Cossi, J. M. Millam, M. Klene, C. Adamo, R. Cammi, J. W. Ochterski, R. L. Martin, K. Morokuma, O. Farkas, J. B. Foresman, and D. J. Fox), Gaussian, Inc. Wallingford CT, **2016**.

FULL PAPER

Entry for the Table of Contents

Insert graphic for Table of Contents here.



Based on the small-molecule DPP-based fluorophore **T25** with NIR-II and NIR-IIa emission, **T25@F127** were selected for fluorescence angiography and cerebral vascular microscopic imaging of mice with nearly 800 μm penetrating depth and excellent signal-background ratio of 4.07 and 2.26 (at 250 and 400 μm), respectively. Furthermore, **T25@cRGD** with tumor targeting ability could image tiny metastatic tumor on intestine with a small size of 0.3 mm \times 1.0 mm.